Thermal structure of an exoplanet atmosphere from phase-resolved emission spectroscopy

Kevin B. Stevenson *et al.*

Science **346**, 838 (2014);
DOI: 10.1126/science.1256758

Science (print ISSN 0036-8075; online ISSN 1095-9203) is published weekly, except the last week in December, by the American Association for the Advancement of Science, 1200 New York Avenue NW, Washington, DC 20005.

EXOPLANET ATMOSPHERE

Thermal structure of an exoplanet atmosphere from phase-resolved emission spectroscopy

Kevin B. Stevenson,[1,13]* Jean-Michel Désert,[2] Michael R. Line,[3] Jacob L. Bean,[1] Jonathan J. Fortney,[3] Adam P. Showman,[4] Tiffany Kataria,[4] Laura Kreidberg,[1] Peter R. McCullough,[5,6] Gregory W. Henry,[7] David Charbonneau,[8] Adam Burrows,[9] Sara Seager,[10] Nikku Madhusudhan,[11] Michael H. Williamson,[7] Derek Homeier[12]

Exoplanets that orbit close to their host stars are much more highly irradiated than their solar system counterparts. Understanding the thermal structures and appearances of these planets requires investigating how their atmospheres respond to such extreme stellar forcing. We present spectroscopic thermal emission measurements as a function of orbital phase ("phase-curve observations") for the highly irradiated exoplanet WASP-43b spanning three full planet rotations using the Hubble Space Telescope. With these data, we construct a map of the planet's atmospheric thermal structure, from which we find large day-night temperature variations at all measured altitudes and a monotonically decreasing temperature with pressure at all longitudes. We also derive a Bond albedo of $0.18^{+0.07}_{-0.12}$ and an altitude dependence in the hot-spot offset relative to the substellar point.

Previous exoplanet phase-curve observations (*1*–*7*) have revealed day-night temperature contrasts and hot-spot offsets relative to the substellar point (the point at which the host star would be perceived to be directly overhead). However, these observations were limited to broadband photometry; therefore, the altitudes probed by the phase curves were not uniquely constrained. Spectroscopic phase curves can break previous degeneracies by permitting us to uniquely identify the main atmospheric opacity source within the observed bandpass and infer the planet's atmospheric temperature-pressure profile as a function of orbital phase (*8*–*12*).

The WASP-43 system contains a transiting Jupiter-size exoplanet on a 19.5-hour orbit around its K4 host star (*13*, *14*). Previous measurements (*14*–*17*) of its dayside thermal emission detected no signs of a thermal inversion and suggested low day-night energy redistribution. However, the precise thermal structure of the dayside atmosphere remains unknown without higher-resolution observations, and the planet's global energy budget and atmospheric heat-redistribution efficiency are poorly constrained without observations of the nightside.

Over 4 to 7 November 2013, we used the Wide Field Camera 3 (WFC3) instrument from the Hubble Space Telescope (HST) to observe three nearly consecutive orbits of WASP-43b. The planet orbits so close to its host star that it is tidally locked. Therefore, orbital phase is equivalent to rotational phase for the planet, and observations over a complete orbit allow us to map the entire surface of the planet. HST also acquired data for three primary transits and two secondary eclipses, where the planet passes in front of and behind its host star, respectively, between 9 November 2013 and 5 December 2013.

[1]Department of Astronomy and Astrophysics, University of Chicago, 5640 South Ellis Avenue, Chicago, IL 60637, USA. [2]CASA, Department of Astrophysical and Planetary Sciences, University of Colorado, 389-UCB, Boulder, CO 80309, USA. [3]Department of Astronomy and Astrophysics, University of California, Santa Cruz, CA 95064, USA. [4]Department of Planetary Sciences and Lunar and Planetary Laboratory, The University of Arizona, Tucson, AZ 85721, USA. [5]Space Telescope Science Institute, Baltimore, MD 21218, USA. [6]Department of Physics and Astronomy, Johns Hopkins University, 3400 North Charles Street, Baltimore, MD 21218, USA. [7]Center for Excellence in Information Systems, Tennessee State University, Nashville, TN 37209, USA. [8]Department of Astronomy, Harvard University, Cambridge, MA 02138, USA. [9]Department of Astrophysical Sciences, Princeton University, Princeton, NJ 08544, USA. [10]Department of Earth, Atmospheric, and Planetary Sciences, Department of Physics, Massachusetts Institute of Technology, 54-1718, 77 Massachusetts Avenue, Cambridge, MA 02139, USA. [11]Institute of Astronomy, University of Cambridge, Cambridge CB3 OHA, UK. [12]Centre de Recherche Astrophysique de Lyon, UMR 5574, CNRS, Université de Lyon, École Normale Supérieure de Lyon, 46 Allée d'Italie, F-69364 Lyon Cedex 07, France. [13]NASA Sagan Fellow.
*Corresponding author. E-mail: kbs@uchicago.edu

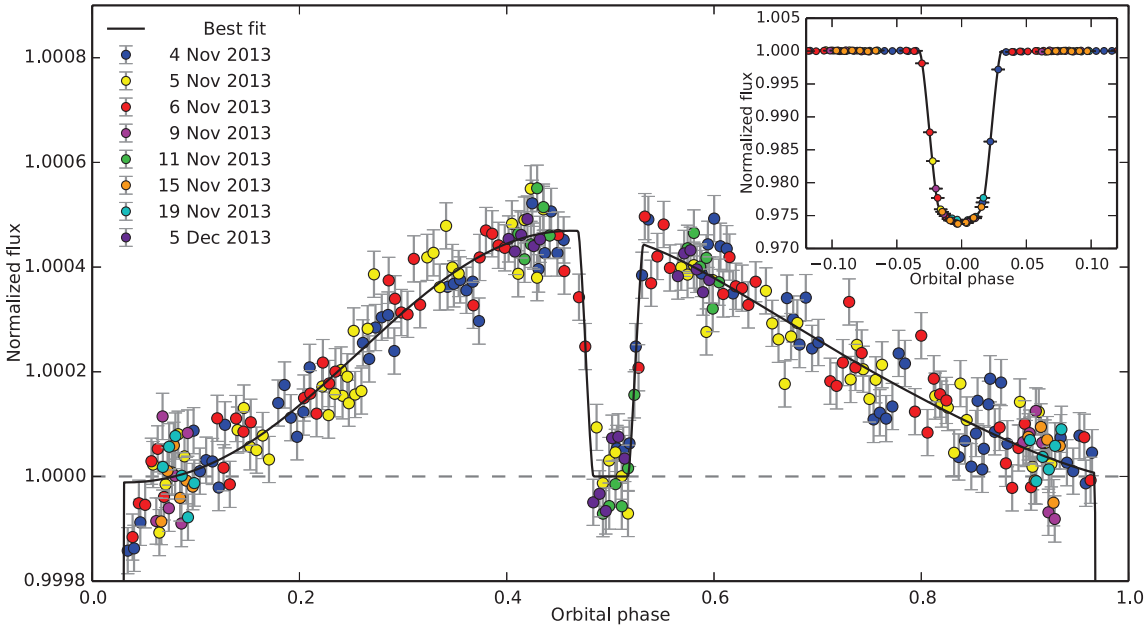

Fig. 1. Band-integrated phase curve of WASP-43b. The systematics-corrected flux values are binned in time, normalized to the stellar flux, and have 1σ error bars. Each color represents data acquired from a different HST visit. The phase curve depicts steadily increasing and decreasing observed flux that originates from different longitudes of the tidally locked planet as it makes one complete rotation. Light from the planet is blocked near an orbital phase of 0.5 as it is eclipsed by its host star. The model phase curve maximum occurs 40 ± 3 min before the midpoint of secondary eclipse, which corresponds to a shift of 12.3 ± 1.0° east of the substellar point. The model phase curve minimum occurs 34 ± 5 min after the primary transit midpoint, or 10.6 ± 1.4° west of the antistellar point. As a result, maximum planetary emission occurs 0.436 ± 0.005 orbits after the observed minimum (for depths probed by these observations) and the shape of the phase curve is asymmetric. Inset, for comparison, is the white light curve primary transit. It is notable that the observed flux values are consistently low for ~30 min after transit egress.

All of the observations used the G141 grism (1.1 to 1.7 μm) and the bidirectional spatial scan mode.

Using custom software (*18*, *19*), we reduced the data and extracted the spectra. We produced time-series spectroscopy by dividing the spectra into 15 0.035-μm-wide channels (7 pixels, resolution $R = \lambda/\Delta\lambda \sim 37$). We also produced band-integrated "white" light curves to resolve finer details in the shape of the phase curve (Fig. 1). We simultaneously fit the light curves using transit and uniform-source eclipse models (*20*), a baseline flux for each HST scan direction, two standard model components for HST orbit-long and visit-long systematics, and a sinusoidal function to represent the phase variation (*19*, *21*). We estimate uncertainties using a differential-evolution Markov-chain Monte Carlo (DE-MCMC) algorithm (*18*) and utilize an independent analysis pipeline (*21*) to confirm our light-curve fits.

The white light phase curve (Fig. 1) reveals a distinct increase in flux as the tidally locked day-side rotates into view. The flux peaks prior to secondary eclipse (eastward of the substellar point) and then decreases until the planet transits in front of its host star. Because the phase curve minimum occurs west of the antistellar point, we detect a strong asymmetry (~10σ) in the shape of the observed phase curve. We measure a white light curve eclipse depth that is consistent with the peak-to-peak planet flux variation. This confirms a relatively cool night side and poor heat redistribution. Table S1 lists our best-fit parameters with uncertainties.

We gain additional information by decomposing the white light phase curve into 15 spectrophotometric channels (Fig. 2). The spectrally resolved phase curves exhibit wavelength-dependent amplitudes, phase shifts, and eclipse depths (table S2). We use the measured phase-resolved emission spectra (Fig. 2C) to infer the temperature structure and molecular abundances at 15 binned orbital phases (each of width 0.0625). We fit atmospheric models to these spectra using a DE-MCMC approach from the CHIMERA Bayesian retrieval suite (*22*). For each phase, a five-parameter, double-gray radiative equilibrium solution parameterizes the planet's temperature structure (*23*). The models include six thermochemically plausible and spectrally prominent absorbers (H_2O, CH_4, CO, CO_2, NH_3, and H_2S). We find that water is the only absorber to significantly influence the phase-resolved emission spectra (*24*) (Fig. 2). The model spectra are in good agreement with the data, achieving a typical χ^2 value of 18 with 15 data points and 6 relevant free parameters (fig. S3).

Using the atmospheric models to estimate the day- and night-side fluxes, we find that the planet redistributes heat poorly [(*19*), heat redistribution factor $\mathcal{F} = 0.503^{+0.021}_{-0.003}$, where $\mathcal{F} = 0.5 \rightarrow 1$ spans the range from zero to full heat redistribution]. This is predicted to occur when the radiative time scale is shorter than the relevant dynamical time scales, including those for wave propagation and advection over a hemisphere (*25*). Poor redistribution has been inferred before, but only for hot Jupiters receiving significantly greater stellar flux than WASP-43b (*4*, *7*). We estimate the fraction of incident stellar light reflected by WASP-43b's atmosphere by computing the day- and night-side bolometric fluxes from the model spectra and find a Bond albedo of $0.18^{+0.07}_{-0.12}$. This

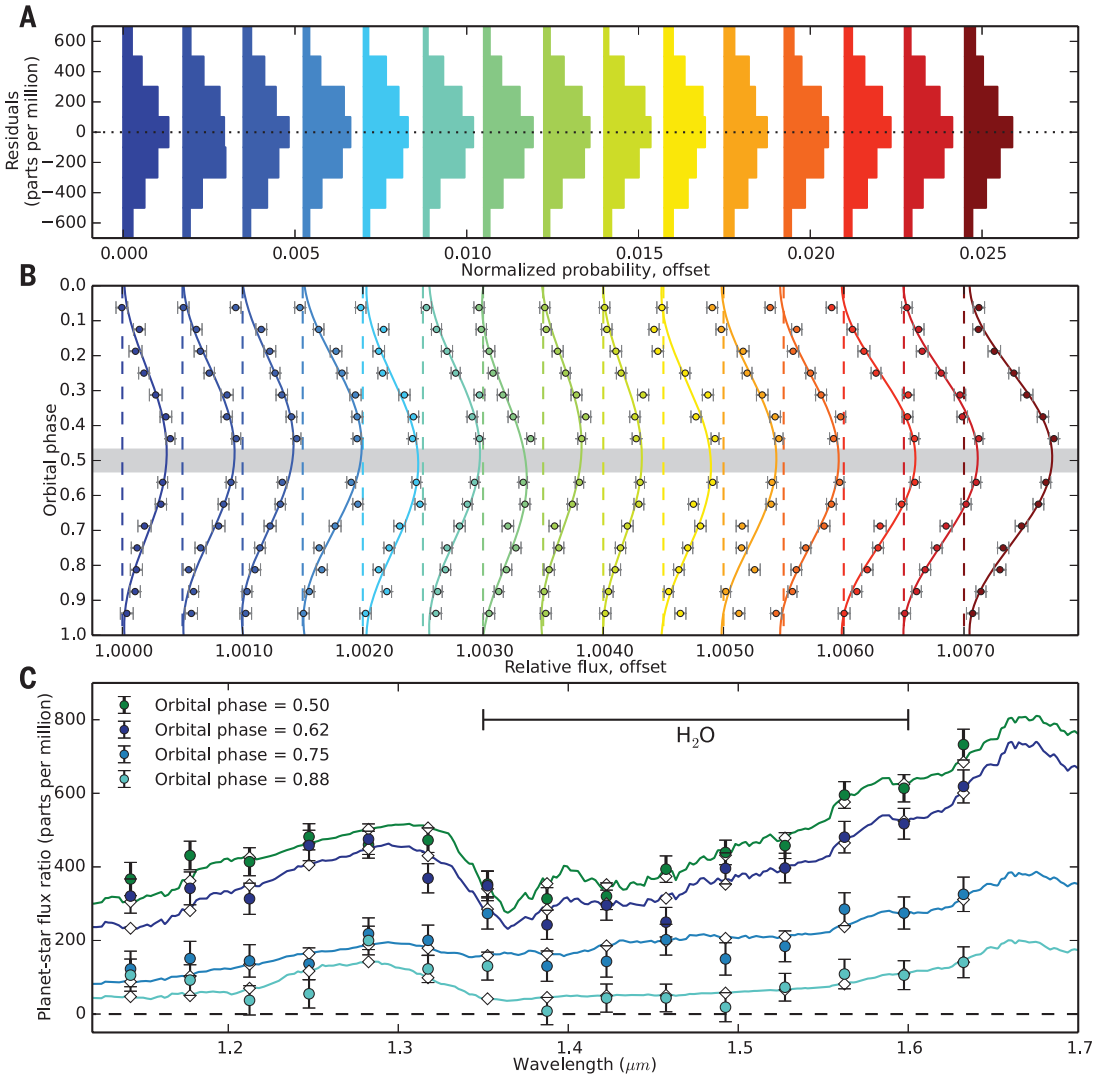

Fig. 2. Phase-resolved emission spectrum of WASP-43b relative to the stellar flux. (**A**) The histograms of the unbinned phase-curve residuals are separated horizontally by wavelength [colors, defined on the abscissa of (C)] for clarity. The residuals are Gaussian distributed with a zero mean and show no evidence of correlated noise. (**B**) We show binned phase curves (colored points with 1σ error bars) and best-fit models (colored lines). The planet emission is normalized with respect to the stellar flux and separated horizontally by wavelength for clarity. The gray region depicts the time of secondary eclipse. (**C**) We illustrate a subset of data points from (B), except plotted as a function of wavelength and with best-fit atmospheric models (colored lines). White diamonds depict the models binned to the resolution of the data. For clarity, we only display planet-to-star flux ratios at four planet phases: full (0.5, secondary eclipse), waning gibbous (0.62), half (0.75), and waning crescent (0.88). In figs. S1 to S3, we provide full 1D and 2D representations of (B) and (C). A time-lapse video of the planet's phase-resolved emission spectrum is available in movie S1.

method assumes energy balance with the parent star but requires no detection of reflected light (*19*). The low Bond albedo is consistent with model predictions that hot Jupiters absorb most of the flux incident upon them (*11*, *26*, *27*).

The atmospheric model fits reveal information about WASP-43b's phase-dependent thermal structure at the pressure levels probed by these observations (Fig. 3). Depending on the wavelength and phase, these pressures range from 0.01 to 1 bar (fig. S4). The retrieved thermal profiles are consistent with a global, monotonically decreasing temperature with altitude, as would be expected from radiative cooling without high-altitude absorbers of stellar radiation. As a test, we compare the retrieved dayside-averaged thermal profile to three scenarios of self-consistent radiative equilibrium models (*28*) and find that it is most congruous with the thermal structure expected at the substellar point (fig. S5). This result supports our findings of a low day-night heat redistribution.

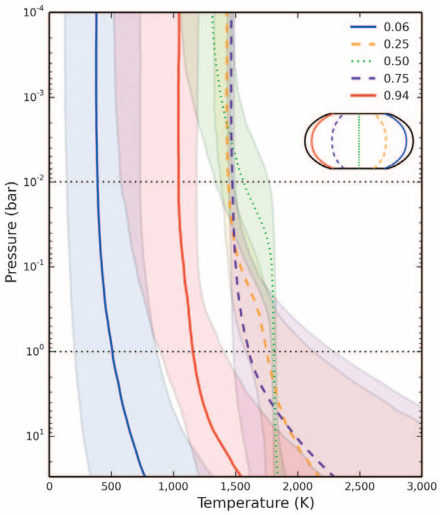

Fig. 3. Thermal profiles of WASP-43b at select orbital phases. Higher pressures indicate deeper within the planet's atmosphere. Colored curves depict median values with 1σ uncertainty regions for the assumed parameterization of the retrieval. We illustrate the temperature asymmetry on the planet's night side immediately before and after transit (orbital phase = 0.06 and 0.94), the similar thermal profiles on WASP-43b's morning and evening terminators (0.25 and 0.75), and the dayside-averaged profile (0.5). The HST/WFC3 measurements probe the atmosphere primarily between 0.01 and 1.0 bar (horizontal dotted lines). The retrieved model profiles are 1D representations of the disk-integrated flux values at each phase. However, because the emitted flux values at these wavelengths are near the peak of the Planck curve, the flux scales as T^5 or more and the disk-integrated thermal profiles are heavily weighted toward the hotter dayside. As a result, there is no significant change in the modeled temperature structure over half of the orbital phases (0.25 → 0.75, when the substellar point is visible). We plot individual pressure-temperature profiles with 1σ uncertainty regions in fig. S4. A time-lapse video of WASP-43b's phase-resolved thermal profile is available in movie S1.

Adopting the same sinusoidal function used to fit the phase variation (*19*), we invert the spectroscopic light curves into longitudinally resolved brightness temperature maps (*29*) (Fig. 4). The brightness temperature, T_B, is a function of atmospheric opacity, and water vapor is the main source of opacity in this bandpass. Because T_B is systematically cooler within the water band, this signifies the global presence of water vapor within the pressure regions probed by these measurements (fig. S7).

The large measured day-night luminosity difference of WASP-43b [(*19*), $L_{day}/L_{night} > 20$ at 1σ, mode ~ 40] contrasts sharply with the modest day-night differences inferred from Spitzer Space Telescope photometry for giant planets such as HD 189733b, HD 209458b, and HD 149026b that are similarly irradiated (*1*, *5*, *25*). Unlike Spitzer data, our spectrum samples the planet's flux near the peak of its Planck curve, allowing for a more robust determination of the total dayside luminosity. This data set suggests that derived day-night differences may be strongly wavelength dependent and that mid-infrared photometry may not give a complete picture of planetary circulation.

Brightness temperature maps, being functions of both longitude and atmospheric depth, reveal the dynamics of a planet's atmosphere. Phase-curve peaks prior to the time of secondary eclipse (as seen in Fig. 1) have previously been reported in hot Jupiters (*1*, *6*) and match predictions from three-dimensional (3D) circulation models (*30*–*32*). Such models show that the eastward offset results from a strong jet stream at the equator; our observations thus suggest that WASP-43b exhibits such an eastward-flowing jet. Our spectrophotometric observations further demonstrate the influence of water vapor on the emergent thermal structure. Inside the water band (1.35 to

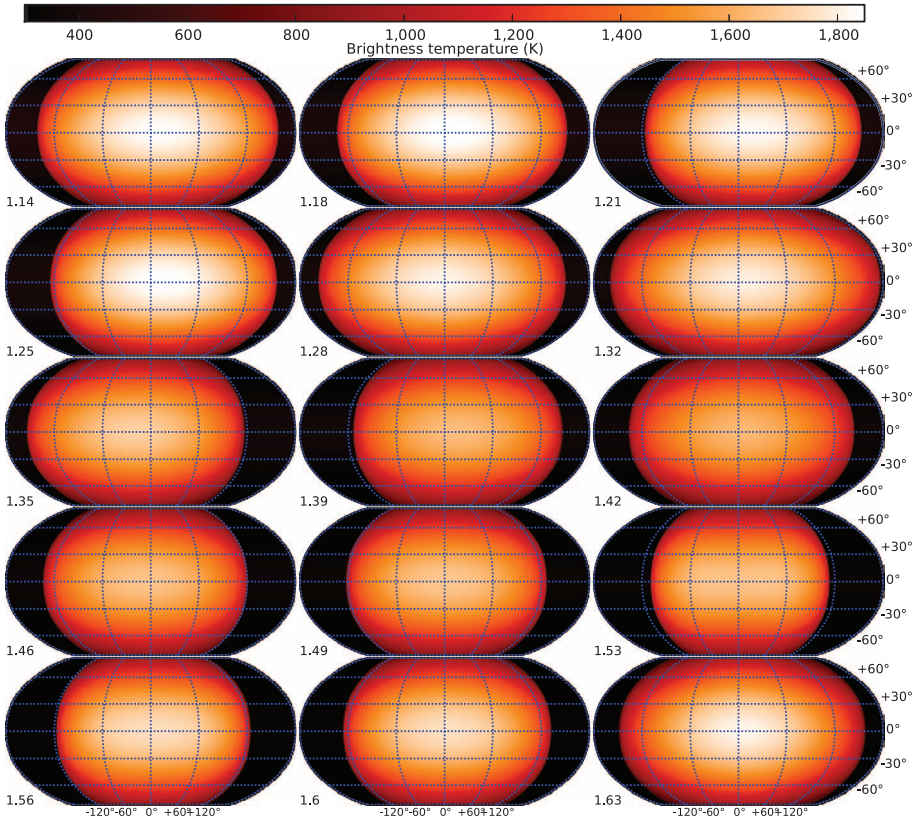

Fig. 4. Longitudinally resolved brightness temperature maps of WASP-43b in all 15 spectrophotometric channels. Black regions in this Robinson projection indicate no discernible contribution. Numbers indicate the wavelength (in micrometers). The observations constrain the brightness temperature at each longitude, but contain no latitudinal information (we assign a $\cos^2$ weighting). In general, the change in temperature is relatively small over the planet's dayside (−90° to +90°) and comparatively extreme near ±120°, thus indicating that we detect emission over the planet's entire dayside. Because WASP-43b does not contain a thermal inversion at these pressures, the hotter regions at a given longitude sample deeper within the atmosphere. The presence of water vapor in the planet's atmosphere explains the relatively cool brightness temperature from 1.35 to 1.6 μm. Outside of the water feature, the brightness temperature peak (indicated in white) is predominantly eastward (toward positive longitudes) of the substellar point. This correlation is readily seen in fig. S8 and matches the predictions of 3D circulation models. Figure S6 displays 1D brightness temperatures with uncertainty regions.

1.6 μm), observations probe lower atmospheric pressures (higher altitudes), and we measure smaller phase-curve peak offsets relative to the other wavelengths (figs. S7 and S8). This is qualitatively consistent with variable brown dwarf measurements (*33*) and circulation-model predictions (*25*, *31*, *32*, *34*), which show that smaller displacements are expected at higher altitudes where radiative time scales are much shorter than the relevant dynamical time scales. However, the observed westward offset of the coldest regions from the antistellar point is puzzling and is not predicted by most models.

The strong day-night temperature variation observed for WASP-43b distinguishes itself from the predominantly uniform temperatures of the solar system giant planets. This illustrates the importance of radiative forcing on the atmospheres of close-in exoplanets. Phase-resolved emission spectroscopy offers a unique way to determine how the extreme stellar radiation incident on these planets is absorbed, circulated, and reemitted. This approach represents a new opportunity for future observations to constrain theories of planetary atmospheric dynamics in a new regime.

REFERENCES AND NOTES

1. H. A. Knutson *et al.*, *Nature* **447**, 183–186 (2007).
2. H. A. Knutson *et al.*, *Astrophys. J.* **703**, 769–784 (2009).
3. I. J. M. Crossfield *et al.*, *Astrophys. J.* **723**, 1436–1446 (2010).
4. N. B. Cowan *et al.*, *Astrophys. J.* **747**, 82 (2012).
5. H. A. Knutson *et al.*, *Astrophys. J.* **754**, 22 (2012).
6. N. K. Lewis *et al.*, *Astrophys. J.* **766**, 95 (2013).
7. P. F. L. Maxted *et al.*, *Mon. Not. R. Astron. Soc.* **428**, 2645–2660 (2013).
8. S. Seager, D. D. Sasselov, *Astrophys. J.* **502**, L157–L161 (1998).
9. A. Burrows *et al.*, *Astrophys. J.* **534**, L97–L100 (2000).
10. T. Guillot, A. P. Showman, *Astron. Astrophys.* **385**, 156–165 (2002).
11. D. Sudarsky, A. Burrows, I. Hubeny, *Astrophys. J.* **588**, 1121–1148 (2003).
12. J. J. Fortney, C. S. Cooper, A. P. Showman, M. S. Marley, R. S. Freedman, *Astrophys. J.* **652**, 746–757 (2006).
13. C. Hellier *et al.*, *Astron. Astrophys.* **535**, L7 (2011).
14. M. Gillon *et al.*, *Astron. Astrophys.* **542**, A4 (2012).
15. W. Wang *et al.*, *Astrophys. J.* **770**, 70 (2013).
16. G. Chen *et al.*, *Astron. Astrophys.* **563**, A40 (2014).
17. J. Blecic *et al.*, *Astrophys. J.* **781**, 116 (2014).
18. K. B. Stevenson *et al.*, *Astron. J.* **147**, 161 (2014).
19. Materials and methods are available as supplementary materials on *Science* Online.
20. K. Mandel, E. Agol, *Astrophys. J.* **580**, L171–L175 (2002).
21. L. Kreidberg *et al.*, *Nature* **505**, 69–72 (2014).
22. M. R. Line, H. Knutson, A. S. Wolf, Y. L. Yung, *Astrophys. J.* **783**, 70 (2014).
23. V. Parmentier, G. Guillot, *VizieR Online Data Catalog* **356**, 29133 (2013).
24. L. Kreidberg *et al.*, *Astrophys. J.* **793**, L27 (2014).
25. D. Perez-Becker, A. P. Showman, *Astrophys. J.* **776**, 134 (2013).
26. M. S. Marley, C. Gelino, D. Stephens, J. I. Lunine, R. Freedman, *Astrophys. J.* **513**, 879–893 (1999).
27. A. Burrows, L. Ibgui, I. Hubeny, *Astrophys. J.* **682**, 1277–1282 (2008).
28. J. J. Fortney, K. Lodders, M. S. Marley, R. S. Freedman, *Astrophys. J.* **678**, 1419–1435 (2008).
29. N. B. Cowan, E. Agol, *Astrophys. J.* **678**, L129–L132 (2008).
30. A. P. Showman, T. Guillot, *Astron. Astrophys.* **385**, 166–180 (2002).
31. C. S. Cooper, A. P. Showman, *Astrophys. J.* **629**, L45–L48 (2005).
32. A. P. Showman *et al.*, *Astrophys. J.* **699**, 564–584 (2009).
33. E. Buenzli *et al.*, *Astrophys. J.* **760**, L31 (2012).
34. A. Burrows, E. Rauscher, D. S. Spiegel, K. Menou, *Astrophys. J.* **719**, 341–350 (2010).

ACKNOWLEDGMENTS

This work is based on observations made with the NASA–European Space Agency Hubble Space Telescope that were obtained at the Space Telescope Science Institute (STScI), which is operated by the Association of Universities for Research in Astronomy, Inc., under NASA contract NAS 5-26555. Data are available through the Mikulski Archive for Space Telescopes (MAST). We thank A. Vick and M. Reinhart of STScI for scheduling these observations, which are associated with program GO-13467. Support for this work was provided by NASA through a grant from the STScI, the Sagan Fellowship Program (to K.B.S.) as supported by NASA and administered by the NASA Exoplanet Science Institute (NExScI), the Alfred P. Sloan Foundation through a Sloan Research Fellowship (to J.L.B.), and the NSF through a Graduate Research Fellowship (to L.K.). G.W.H. and M.H.W. acknowledge long-term support from NASA, NSF, Tennessee State University, and the State of Tennessee through its Centers of Excellence program. S.S. acknowledges funding from the Massachusetts Institute of Technology. D.H. acknowledges support from the European Research Council under the European Community's Seventh Framework Programme—FP7/2007—2013 grant agreement no. 247060.

SUPPLEMENTARY MATERIALS

www.sciencemag.org/content/346/6211/838/suppl/DC1
Materials and Methods
Supplementary Text
Tables S1 and S2
Figs. S1 to S8
Movie S1

30 May 2014; accepted 17 September 2014
Published online 9 October 2014;
10.1126/science.1256758

SEXUAL CONFLICT

The evolution of infanticide by males in mammalian societies

Dieter Lukas[1]* and Elise Huchard[1,2]

Male mammals often kill conspecific offspring. The benefits of such infanticide to males, and its costs to females, probably vary across mammalian social and mating systems. We used comparative analyses to show that infanticide primarily evolves in social mammals in which reproduction is monopolized by a minority of males. It has not promoted social counterstrategies such as female gregariousness, pair living, or changes in group size and sex ratio, but is successfully prevented by female sexual promiscuity, a paternity dilution strategy. These findings indicate that infanticide is a consequence, rather than a cause, of contrasts in mammalian social systems affecting the intensity of sexual conflict.

Infanticide by males is widespread in mammals and may be the main cause of infant mortality in some populations (*1*). It has long been viewed as a sexually selected strategy that increases mating opportunities for killer males by shortening postpartum infertility in the victim's mother (*2*, *3*). This is supported by natural observations across taxa showing that males target unrelated infants and often impregnate the victim's mother afterward (*1*, *3*, *4*). Attempts to explain the taxonomic distribution of infanticide have, however, been mainly limited to investigations of the life-history correlates of male infanticide (*5*–*8*), showing that it rarely occurs where it does not accelerate the mother's return to sexual activity, as in seasonal breeders who cannot resume cycling before the next breeding season (*8*).

Several scenarios have linked the distribution of infanticide across species to the evolution of social organization and mating systems in mammals, and they remain largely untested or disputed (*9*, *10*). According to the sexual selection hypothesis, the distribution of infanticide is expected to be modulated by contrasts in social systems that affect the intensity of male intrasexual competition (*3*, *5*, *8*). Male infanticide should thus be prevalent in species in which a few males mate with multiple females and monopolize most reproductive opportunities. However, females may respond to infanticide by developing counterstrategies that may refine patterns of associations across species. Social counterstrategies may include the evolution of female sociality (*6*, *11*, *12*), of permanent male-female associations (*13*–*15*), or of changes in the group sex ratio (*6*, *11*, *12*, *15*), because females may form coalitions with other females or with resident males to defend their progeny against male invaders. Additionally, females may mate with multiple partners to confuse paternity and dissuade infanticide (*6*, *16*, *17*), which may thus be absent in species with pronounced sperm competition. The evolutionary arms race between the sexes driven by male infanticide has generated confusion and controversy regarding the role of infanticide in the evolution of mammalian societies, calling for more integrative studies.

We used information gathered on 260 mammal species, including 119 species with and 141 without infanticide (Fig. 1), to perform phylogenetic analyses (*18*) to identify how variation in social organization and mating systems may have favored or prevented the evolution of infanticide by males. Specifically, we tested whether

[1]Large Animal Research Group, Department of Zoology, University of Cambridge, Downing Street, Cambridge CB2 3EJ, UK. [2]Centre d'Ecologie Fonctionnelle et Evolutive, UMR 5175, CNRS – Université de Montpellier, 1919 Route de Mende, 34293 Montpellier Cedex 5, France.
*Corresponding author. E-mail: dl384@cam.ac.uk